Numerical and Experimental Analysis of the Fluid-Structure Interaction in Presence of a Hyperelastic Body

H. Esmailzadeh[1]
Mechanical Engineering Department,
Ferdowsi University of Mashhad,
Mashhad 91775-1111, Iran
e-mail: esmailzadeh_hamed@yahoo.com

M. Passandideh-Fard
Associate Professor
Mechanical Engineering Department,
Ferdowsi University of Mashhad,
Mashhad 91775-1111, Iran
e-mail: mpfard@um.ac.ir

In this study, a numerical algorithm is developed for simulating the interaction between a fluid and a 2D/axisymmetric hyperelastic body based on a full Eulerian fluid-structure interaction (FSI) method. In this method, the solid volume fraction is used for describing the multicomponent material and the deformation tensor for describing the deformation of the hyperelastic body. The core elements of the simulation method are the constitutive law in the Cauchy stress form and an equation for the transport of the deformation tensor field. A semi-implicit formulation is used for the elastic stress to avoid instability especially for solid with high stiffness. The strain rate has a discontinuity across the fluid/solid interface. For improving the accuracy in capturing the interface, solid is treated as a highly viscous fluid. The viscosity term has the effect of smoothing the velocity and keeping the simulation stable. An experimental setup is used to validate the numerical results. The movement of a sphere made of silicone in air and its impact on a rigid substrate are investigated. The images are captured using a high speed CCD camera and the image processing technique is employed to obtain the required data from the images. For all cases considered, the results are in good agreement with those of the experiment performed in this study and other numerical results reported in the literature.
[DOI: 10.1115/1.4027893]

Keywords: fluid-structure interaction, numerical simulation, volume of fluid (VOF), hyperelastic material, implicit elastic term, image processing

1 Introduction

FSI appears in many applications such as animation, biological systems, and industrial processes. The FSI has been used in computer graphics and motion picture arts for many years. It has also been utilized in life sciences to account for the analysis of aneurysm in arteries and artificial heart valves. Moreover, the FSI is a crucial consideration in the design of many engineering systems, e.g., aircraft wings, bridges, turbine blades, etc. where the excitation forces between the fluid and the structure may cause severe damages. Failing to consider the effects of FSIs can be catastrophic, especially in structures comprising materials susceptible to fatigue.

The phenomenon of the FSI has been studied theoretically for more than a century. These problems, however, pose a great challenge because they involve complex moving boundaries and need the simultaneous solution of the equations for nonlinear elasticity and nonlinear fluid mechanics. The equations to be solved are: governing flow equations; equations of the deformable body; and equations for tracking the fluid/solid interface. Further complexity of the problem is due to the deforming fluid/solid interface where accurate boundary conditions should be applied. Therefore, computationally effective strategies for both the fluid and the solid have to be considered. Computationally speaking, the fluid dynamic problems are modeled in an Eulerian system of coordinate, while the structure dynamic analyses are normally performed in a Lagrangian system.

Numerical methods for solving the FSI are classified in three major methods: Lagrangian–Lagrangian, Eulerian–Lagrangian, and Eulerian–Eulerian. The Lagrangian–Lagrangian method treats the fluid and the structure as two computational fields which can be solved separately with their respective mesh discretization and numerical algorithm. The interfacial conditions are used explicitly to communicate the information between the fluid and the structure solutions. In this method, the fluid/solid interface is modeled using a fitted unstructured grid which has the advantage that the moving boundary condition is satisfied more accurately. Pure Lagrangian methods provide flexibility in spatial meshing and can conveniently catch the detailed physics along the fluid/solid interface. The major drawbacks of these methods, however, are the difficulties in data exchange between the two domains of fluid and solid along the interface, the lack of temporal convergence, and especially the inconsistency between numerical codes used for the fluid and solid. The pure Lagrangian method was employed by Belytschko and Kennedy [1] and Donea et al. [2] to study hydrostructural problems. A more accurate approach of this method is called the arbitrary Lagrangian–Eulerian (ALE) [3,4], which is less restrictive because of the moving grid that follows the deformable boundaries. A characteristic property inherent to the ALE method is the ability to adjust to a surface of a body leading to simulations results with a high-order of accuracy. This method is used for applications such as blood flow [5], moving rigid particles [6], and moving hyperelastic particles [7]. The main difficulty associated with the ALE method is that the whole computational domain has to be remeshed as the object moves or deforms.

[1]Corresponding author.

Contributed by the Fluids Engineering Division of ASME for publication in the JOURNAL OF FLUIDS ENGINEERING. Manuscript received July 28, 2013; final manuscript received June 18, 2014; published online September 4, 2014. Assoc. Editor: Zhongquan Charlie Zheng.

In the Eulerian–Lagrangian methods, an Eulerian background mesh is used for the fluid and a Lagrangian moving mesh for the solid. In this method, the fluid is assumed to occupy the entire computational domain with a fixed mesh. The solid, however, is assumed as a certain volume in the fluid mesh and its development is described with accurate constitutive equations. As the solid moves in the computational domain, its corresponding mesh is varying in time. The interfacial conditions are implicit in the solution procedure. In other words, Eulerian–Lagrangian methods treat the boundary location and the related interface conditions as constraints imposed on the equations. This method can be derived from the theorem of Lagrange multipliers [8]; these multipliers in most cases appear as source (or force) terms in the fluid equation. Thus, in these methods, computation of the Lagrange multipliers is essential and directly affects the accuracy of the fluid and solid solutions. Most of these methods are based on the immersed algorithms which are classified as the FSI methods that add force terms to fluid equations to represent the FSI [9]. A well-known algorithm called the immersed boundary method (IBM) was originally introduced by Peskin [10] to study the flow in a heart valve. The idea was useful in solving the FSI problems with a free movement of solid through a fluid domain. The interaction between the fluid and the deformable body is treated through nodal forces incorporated in the momentum equations. These forces (external terms) that satisfy the boundary conditions on the surface are applied over the computational domain through smoothed approximation of the Dirac delta function. Inspired by the work of Peskin [10], other researchers applied various forms of the IBM method in a wide variety of FSI problems. Wang and Liu [11] proposed extended immersed boundary method (EIBM) that has several distinct features in comparison with the IBM. The extensions in the EIBM method were beneficial to the accurate modeling of complex biological systems. Gilmanov and Acharya [12] utilized the hybrid immersed boundary method to study the behavior of a capsule in shear flow and the falling of rigid and flexible sphere in a fluid zone. The IBM model uses the discrete delta function which smears out a sharp interface into a thickness of order of the mesh width. Le et al. [13] employed the immersed interface method (IIM) to avoid smearing a sharp interface and maintain the accuracy by incorporating certain jumps in velocity and pressure into the finite difference scheme near the interface. Based on these conditions, the fluid and solid motions are coupled in the interface by the no-slip condition and the balance of dynamic forces. This method can handle rigid immersed boundaries, fluid-membrane interactions and membrane–membrane interactions. Glowinski et al. [14] introduced the fictitious domain method in which a new Lagrange multiplier is presented for the direct numerical simulation of flow with suspended solid particles. In the Eulerian–Lagrangian methods, the restrictions inherent to pure Lagrangian methods are absent; therefore, these methods are more stable compared to the Lagrangian–Lagrangian methods. However, Eulerian–Lagrangian methods are less accurate compared to the pure Lagrangian methods and require more sophisticated computational programming.

In both pure Lagrangian and Eulerian–Lagrangian methods, to predict the motion and deformation of a solid body, the solid displacement is temporally updated in a Lagrangian manner. Depending on the complexity and number of the solid objects, the remeshing procedure in each time step may lead to extensive computations. In order to alleviate this difficulty in the FSI simulations, another method called the Eulerian–Eulerian method has been proposed where a fixed mesh is used for both fluid and solid. In contrast to the Lagrangian method where the solid deformation is tracked based on the solid mesh displacements, in the Eulerian approach, the mesh is fixed and a deformation tensor is employed [15,16]. This deformation tensor is updated temporally and as a result the remeshing is not necessary. In the Eulerian–Eulerian method, stresses in the solid object are calculated from velocity gradient instead of displacements. Sugiyama et al. [17] used a FSI model based on an Eulerian framework to study biconcave neo-Hookean particles in a Poiseuille flow [17]. In later publications, the same group used this model to study the deformation of hyperelastic bodies in incompressible fluid flow for other applications [18–24]. These applications include: fluid flow in a pressure driven hyperelastic wavy channel [18]; axisymmetric flow inside a neo-Hookean tube subjected to a pressure gradient [21]; pressure-driven flow with the biconcave membrane capsules (red blood cells) [22]; and blood flow including elastic membranes and plateletlike elastic solids in capillary vessel [24].

The method of Sugiyama et al. [19] is capable of handling unprescribed motion of the solid object in the fluid. Once the initial value of the solid volume fraction is known, this method allows the FSI simulation without remeshing in each time step. They used this method to compare their numerical results with those of pure Lagrangian and Eulerian–Lagrangian numerical methods. In the Sugiyama et al. method [19]; however, the strain rate has a discontinuity across the interface which leads to a nonphysical dynamic condition especially for solids with high stiffness or when the solid interacts with a fluid of low density. Furthermore, in their model, the fifth-order weighted essentially nonoscillatory method is used to advect the solid volume fraction field that makes the interface numerically diffusive [19].

In this study, an improved numerical model based on the FSI method of Sugiyama et al. [19] is used to simulate the interaction between a fluid and a 2D/axisymmetric hyperelastic body. To resolve the nonphysical dynamic condition at the fluid/solid interface, a modification is presented in which a high viscosity is attributed to the solid zone. This modification smoothes the velocity field in the solid object, and reduces the effect of elastic stresses at the fluid/solid interface. Therefore, there is no need to incorporate the jump conditions in velocity and pressure into the finite difference scheme as applied in the IIM [13]. It should be emphasized that in treating the solid object as a high viscous fluid in this study, the elastic stresses are considered in the governing equations; i.e., the solid body is treated as a deformable body. This is in contrast to previous studies [25,26] where the solid body was only treated as a high viscous fluid with no deformability. The elastic stresses in the solid body are calculated by the constitutive law of deformable solid object which have only nonzero values in the solid zone. The constitutive equation of deformable solid object is expressed as a function of the deformation tensor which is temporally updated on each grid point using a transport equation. The Youngs piecewise linear interface calculation (PLIC) algorithm [27] is used for describing the multicomponent geometry that suppresses the numerical diffusion; this algorithm is frequently used in the multiphase flow simulations [25]. The numerical results are also compared with those of the experiments performed in this study for the movement of a sphere made of a hyperelastic material (silicone) in air and its impact on to a rigid substrate. The numerical model introduced in this study can easily be applied to other fluid flow solvers dealing with unprescribed motion of deformable solid objects.

2 Mathematical Model

The governing equations considered for the entire computational domain including both fluid and solid are

$$\nabla \cdot V = 0 \tag{1}$$

$$\frac{\partial V}{\partial t} + V \cdot \nabla V = \frac{-\nabla P}{\rho} + \frac{1}{\rho}\nabla \cdot \mu\left[\nabla V + (\nabla V)^T\right] + \frac{\nabla \cdot \tau_e}{\rho} + g \tag{2}$$

where V is the velocity vector, ρ is the density, P is the pressure, μ is the dynamic viscosity, τ_e is the elastic stress, and g is the acceleration due to gravity. As mentioned earlier, the deformable solid body is treated as a fluid with a high viscosity where elastic

stresses are also considered in the solid zone. The solid volume fraction is advected using the volume of fluid (VOF) method by means of a scalar field φ_s, defined as

$$\varphi_s = \begin{cases} 0 & \text{in fluid} \\ 0 <, < 1 & \text{in fluid/solid interface} \\ 1 & \text{in solid} \end{cases} \tag{3}$$

The discontinuity in φ_s is a Lagrangian invariant, propagating according to

$$\frac{D\varphi_s}{Dt} = \frac{\partial \varphi_s}{\partial t} + V \cdot \nabla \varphi_s = 0 \tag{4}$$

The density and viscosity in each cell are defined as

$$\rho = (1 - \varphi_s)\rho_l + \varphi_s \rho_s \tag{5}$$

$$\mu = (1 - \varphi_s)\mu_l + \varphi_s \mu_s \tag{6}$$

The subscripts l and s stand for the fluid and solid, respectively. The Youngs PLIC algorithm [27] is used to advect φ_s based on Eq. (4). The surface tension effects on the fluid/solid interface are neglected.

For a hyperelastic material, the elastic stress τ_e is associated to the strain energy potential W that relies on the hyperelastic constitutive law [28]. For example, the nonlinear Mooney–Rivlin law [19] gives the expression of the hyperelastic stress for solid as

$$\tau_e = 2C_1 B + 2C_2[\text{tr}(B)B - B \cdot B] + 4C_3[\text{tr}(B) - 3]B \tag{7}$$

where B is the left Cauchy-Green deformation tensor and tr(B) represents the trace of tensor B. Sugiyama et al. [19] proposed a modification to the left Cauchy-Green deformation tensor as $\widetilde{B} = \varphi_s^{1/2} B$ to reduce instabilities in the fluid domain. Using this modification, $\widetilde{B}$ is temporally updated on a fixed mesh from the transport equation as

$$\frac{\partial \widetilde{B}}{\partial t} + V \cdot \nabla \widetilde{B} = \nabla V^T \cdot \widetilde{B} + \widetilde{B} \cdot \nabla V \tag{8}$$

with the initial stretch-free condition $\widetilde{B}(t_0) = \varphi_s^{1/2} I$.

However, the strain rate has discontinuity across the fluid/solid interface. This occurs especially when the fluid and solid densities have a large difference or when the solid object has a high stiffness. To improve the accuracy of the model in capturing the interface, a high viscosity is attributed to the solid domain. It has been discussed in more detail elsewhere [25] that the viscosity force has the effect of smoothing the velocity field and maintaining the simulation stable. The improvement in accuracy has been reported in several studies in the literature [25,26,29].

In this study, two cases for a hyperelastic material are considered including neo-Hookean material and Saint Venant-Kirchhoff material. For the neo-Hookean material [15] we have $C_1 = G/2$, $C_2 = C_3 = 0$ and, therefore

$$\tau_e = GB \tag{9}$$

Venant-Kirchhoff material (with large deformations), the coefficients are [19]

$$C_1 = \mu^s_{\text{Lame}}, \quad C_2 = -\frac{\mu^s_{\text{Lame}}}{2}, \quad C_3 = \frac{\lambda^s_{\text{Lame}} + 2\mu^s_{\text{Lame}}}{8} \tag{10}$$

where μ^s_{Lame} and λ^s_{Lame} are the Lame constants related to the stiffness of the Saint Venant-Kirchhoff material.

3 Numerical Method

For discretization of the governing equations, a multistep projection method is used to update velocity based on the flow equations (Eqs. (1) and (2)) and modified left Cauchy-Green deformation tensor based on the transport equation (Eq. (8)).

Step 1:

In the first step, the convective and gravity terms in the momentum equation are discretized using an explicit scheme where an intermediate velocity field V^* is obtained as

$$\frac{V^* - V^n}{\Delta t} = -(V \cdot \nabla V)^n + g^n \tag{11}$$

Step 2:

In the second step, a semi-implicit discretization scheme [25] is used to model the viscous term of the momentum equation to obtain an intermediate velocity $V^{n+1/3}$ as

$$\frac{V^{n+\frac{1}{3}} - V^*}{\Delta t} = \mu \nabla \cdot \left[\frac{\nabla V^{n+\frac{1}{3}} + (\nabla V^T)^{n+\frac{1}{3}}}{\rho^n} \right] \tag{12}$$

which is solved using the tridiagonal matrix algorithm (TDMA) solver to obtain $V^{n+1/3}$.

The semi-implicit treatment of the viscous term based on the above equation allows using a large time step even for simulation of fluids with high viscosities.

Next, based on the transport equation (Eq. (8)), an intermediate deformation tensor $\widetilde{B}^{n+1/3}$ is obtained. For this purpose, the second-order Adams-Bashforth method [20] is applied for the advection term and the Crank–Nicolson method [20] for the velocity gradient terms in the transport equation (Eq. (8)). Based on these schemes, the intermediate deformation tensor $\widetilde{B}^{n+1/3}$ is obtained as

$$\begin{aligned} &\frac{\widetilde{B}^{n+\frac{1}{3}} - \widetilde{B}^n}{\Delta t} + \frac{3}{2} V^n \cdot \nabla \widetilde{B}^n - \frac{1}{2} V^{n-1} \cdot \nabla \widetilde{B}^{n-1} \\ &= \frac{1}{2}\left[(\nabla V^T)^n + (\nabla V^T)^{n+\frac{1}{3}} \right] \cdot \widetilde{B}^n + \frac{1}{2} \widetilde{B}^n \cdot \left[\nabla V^n + \nabla V^{n+\frac{1}{3}} \right] \end{aligned} \tag{13}$$

Based on the $\widetilde{B}^{n+1/3}$ and utilizing Eq. (7), the intermediate elastic stress $\tau_e^{n+1/3}$ is obtained as

$$\begin{aligned} \tau_e^{n+\frac{1}{3}} = {} & 2C_1 \widetilde{B}^{n+\frac{1}{3}} + 2C_2 \left[\text{tr}\left(\widetilde{B}^{n+\frac{1}{3}} \right) \widetilde{B}^{n+\frac{1}{3}} - \widetilde{B}^{n+\frac{1}{3}} \cdot \widetilde{B}^{n+\frac{1}{3}} \right] \\ & + 4C_3 \left[\text{tr}\left(\widetilde{B}^{n+\frac{1}{3}} \right) - 3 \right] \widetilde{B}^{n+\frac{1}{3}} \end{aligned} \tag{14}$$

This term will be used in the next step to model the elastic term of the momentum equation.

Step 3:

In the third step, the elastic term of the momentum equation is discretized with a semi-implicit scheme. To avoid instabilities associated with a high stiff solid object, the method of Ii et al. [20,22] is employed in which a fourth-order Jacobian tensor is utilized to overcome the difficulty associated with the difference between the constitutive laws of the solid and fluid. Based on this method, an intermediate velocity $V^{n+2/3}$ is obtained as

$$\frac{V^{n+\frac{2}{3}}-V^{n+\frac{1}{3}}}{\Delta t}=\frac{1}{2}\nabla\cdot\left[\frac{\tau_e^{n+\frac{1}{3}}+\tau_e^{n+\frac{2}{3}}}{\rho^n}\right] \tag{15}$$

The elastic stress $\tau_e{}^{n+2/3}$ is evaluated by introducing the fourth-order Jacobian tensor $J=[\partial\tau_e(\widetilde{B})/\partial\widetilde{B}]$ as

$$\tau_e^{n+\frac{2}{3}}=\tau_e^{n+\frac{1}{3}}+J^{n+\frac{1}{3}}:\left(\widetilde{B}^{n+\frac{2}{3}}-\widetilde{B}^{n+\frac{1}{3}}\right) \tag{16}$$

Based on the transport equation (Eq. (8)) and similar to Eq. (13), the intermediate deformation tensor $\widetilde{B}^{n+2/3}$ is obtained as

$$\begin{aligned}&\frac{\widetilde{B}^{n+\frac{2}{3}}-\widetilde{B}^{n}}{\Delta t}+\frac{3}{2}V^n\cdot\nabla\widetilde{B}^n-\frac{1}{2}V^{n-1}\cdot\nabla\widetilde{B}^{n-1}\\&=\frac{1}{2}\left[\left(\nabla V^T\right)^n+\left(\nabla V^T\right)^{n+\frac{2}{3}}\right]\cdot\widetilde{B}^n+\frac{1}{2}\widetilde{B}^n\cdot\left[\nabla V^n+\nabla V^{n+\frac{2}{3}}\right]\end{aligned} \tag{17}$$

By subtracting Eq. (13) from Eq. (17), we will have

$$\begin{aligned}\widetilde{B}^{n+\frac{2}{3}}-\widetilde{B}^{n+\frac{1}{3}}=\frac{\Delta t}{2}\Big\{&\left[\left(\nabla V^T\right)^{n+\frac{2}{3}}-\left(\nabla V^T\right)^{n+\frac{1}{3}}\right]\cdot\widetilde{B}^n\\&+\widetilde{B}^n\cdot\left[\nabla V^{n+\frac{2}{3}}-\nabla V^{n+\frac{1}{3}}\right]\Big\}\end{aligned} \tag{18}$$

By substituting Eq. (18) into Eq. (16) and the resulting equation into Eq. (15), a linear system for $V^{n+2/3}$ is obtained as

$$\begin{aligned}\frac{V^{n+\frac{2}{3}}-V^{n+\frac{1}{3}}}{\Delta t}=&\nabla\cdot\left[\frac{\Delta t}{4\rho^n}H\left(V^{n+\frac{2}{3}},\widetilde{B}^n,J^{n+\frac{1}{3}}\right)\right]\\&-\nabla\cdot\left[\frac{\Delta t}{4\rho^n}H\left(V^{n+\frac{1}{3}},\widetilde{B}^n,J^{n+\frac{1}{3}}\right)\right]+\nabla\cdot\left[\frac{\tau_e^{n+\frac{1}{3}}}{\rho^n}\right]\end{aligned} \tag{19}$$

where

$$H\left(V,\widetilde{B},J\right)=J:\left(\nabla V^T\cdot\widetilde{B}+\widetilde{B}\cdot\nabla V\right) \tag{20}$$

To solve the resulted system of equations (Eq. (19)), the TDMA solver is used one more time to calculate $V^{n+2/3}$. Equation (18) is then can be used to compute the intermediate deformation tensor $\widetilde{B}^{n+2/3}$.

Step 4:

In the four step, the pressure term of the momentum equation is modeled implicitly as

$$\frac{V^{n+1}-V^{n+\frac{2}{3}}}{\Delta t}=-\frac{\nabla P^{n+1}}{\rho^n} \tag{21}$$

The continuity equation is also satisfied for the velocity field at the new time step

$$\nabla\cdot V^{n+1}=0 \tag{22}$$

Taking the divergence of Eq. (21) and substituting from Eq. (22) results in a pressure Poisson's equation as

$$\nabla\cdot\left[\frac{1}{\rho^n}\nabla p^{n+1}\right]=\frac{\nabla\cdot V^{n+\frac{2}{3}}}{\Delta t} \tag{23}$$

The resulting set of equations (Eq. (23)) is symmetric and positive definite; a solution is obtained using an incomplete Cholesky-conjugate gradient (LDL^T) solver [30]. In Eq. (23), the density remains within the divergence operator in order to have a smooth pressure distribution across the cells which are in the fluid/solid interface and which numerically are characterized by $\nabla\rho\neq 0$. The obtained pressure field can then be used to find the final velocity field by applying Eq. (21). Based on the transport equation (Eq. (8)) and similar to Eq. (13) the final deformation tensor $\widetilde{B}^{n+1}$ is obtained as

$$\begin{aligned}&\frac{\widetilde{B}^{n+1}-\widetilde{B}^{n}}{\Delta t}+\frac{3}{2}V^n\cdot\nabla\widetilde{B}^n-\frac{1}{2}V^{n-1}\cdot\nabla\widetilde{B}^{n-1}\\&=\frac{1}{2}\left[\left(\nabla V^T\right)^n+\left(\nabla V^T\right)^{n+1}\right]\cdot\widetilde{B}^n+\frac{1}{2}\widetilde{B}^n\cdot\left[\nabla V^n+\nabla V^{n+1}\right]\end{aligned} \tag{24}$$

By subtracting Eq. (17) from Eq. (24), we will have

$$\begin{aligned}\widetilde{B}^{n+1}-\widetilde{B}^{n+\frac{2}{3}}=\frac{\Delta t}{2}\Big\{&\left[\left(\nabla V^T\right)^{n+1}-\left(\nabla V^T\right)^{n+\frac{2}{3}}\right]\cdot\widetilde{B}^n\\&+\widetilde{B}^n\cdot\left[\nabla V^{n+1}-\nabla V^{n+\frac{2}{3}}\right]\Big\}\end{aligned} \tag{25}$$

The above numerical procedure in each time step of the calculation is also presented as a flowchart given in Fig. 1.

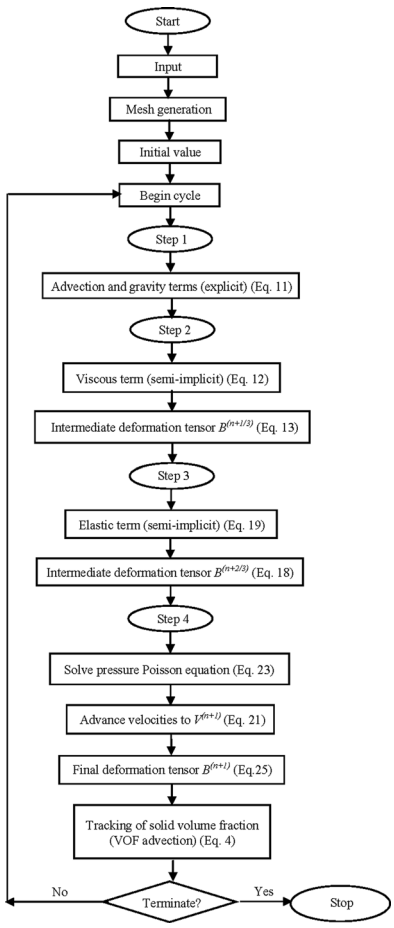

Fig. 1 Flowchart of the sequence of the computational cycle for velocity, deformation tensor, and solid volume fraction

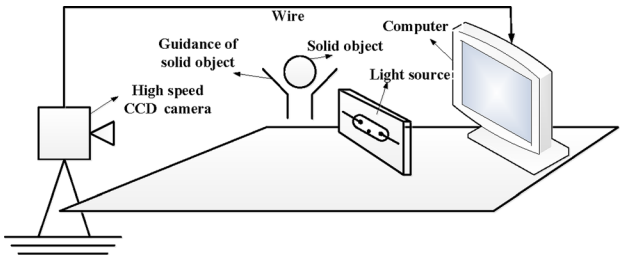

Fig. 2 Schematic of the experimental setup for the motion and impact of a hyperelastic sphere onto a rigid substrate

4 Experimental Setup

To validate the numerical model, the simulation results are compared with those of the simple experiment performed in this study and those of the other models available in the literature. In this study, a simple experiment was setup where the movement of a hyperelastic solid sphere is photographed. A sphere made of silicone as a hyperelastic material, moves in air and impacts on a rigid substrate; it then bounces back and moves upward. A high speed CCD camera, Grasshopper model, made in Point Grey Company, Canada, was used for taking high quality images of various positions of solid object. Figure 2 shows the schematic of the experimental setup. The MATLAB software is employed for image processing and the required information is obtained from the images with a numerical code written in this software.

In the image processing method, first an image involving a certain piece with known dimension is utilized for calibration (Fig. 3(*a*)). The image is read in the MATLAB software and its contrast and brightness are modified to reduce the noises in the image. The image is composed of many pixels which have different colors (values). Using the commands in the toolbox of image processing, every pixel whose color value is larger than a threshold value is set to be white color in the surrounded fluid (air). The remaining pixels located inside the solid object and calibration piece are set to be black color. Having known the size of the calibration piece, the scale factor for all subsequent images (Fig. 3(*b*)) is found. The image processing method is then performed for these images as follows. For the images of the sphere moving in air (before or after the impact) using commands in toolboxes of the MATLAB software, the pixels of maximum and minimum row of the solid object are specified. Therefore, the position of the center of the sphere volume can be obtained (Fig. 3(*c*)). For the images of the sphere during its impact on the substrate, the fluid/solid and solid/substrate interfaces are first detected to obtain the contact radius of solid with the rigid substrate (Fig. 3(*d*)). Having known the contact radius, the center of the sphere volume is obtained using a command in the MATLAB software that traces the sphere boundary. Following the above procedure for all images taken during an experiment, the center position of the solid object at all times is determined. Since the time of each image is also known, the velocity of the object is then calculated based on the subsequent center positions divided by the corresponding time step.

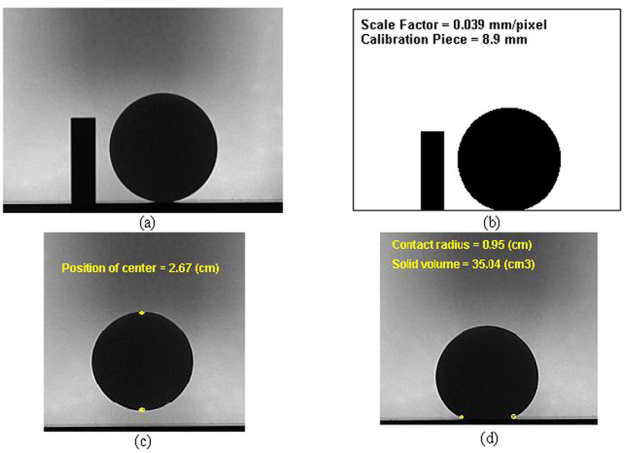

Fig. 3 Iamge processing technique using the MATLAB software to obtain the position of the center of sphere volume: (*a*) image of sphere and a certain piece with known dimension for calibration, (*b*) the image after being processed using a threshold to reveal the sphere and the calibration piece by reducing the color values into black and white, (*c*) the top and bottom pixels of the sphere to obtain the position of its center while moving in air, and (*d*) the detection of the fluid/solid and solid/substrate interfaces to obtain the center during the impact

To provide a brief uncertainty analysis of the experimental measurement, the uncertainties associated with the equipments used in this study are reported in Table 1. The maximum absolute uncertainty for the position and velocity of the solid body measured in the experiments was calculated to be less than 7% in the experiments. More details regarding the uncertainty analysis are given elsewhere [31].

5 Numerical Results

In this section, first, to validate the numerical algorithm, the numerical and experimental results for the motion of a hyperelastic sphere in fluid (air) and its impact onto a rigid substrate are presented. Next, the results of simulations are compared with those of other studies available in the literature for various FSIs. These cases include a soft wall deformed by a fluid flow, a deformable solid motion in a lid-driven cavity, an oscillating soft disk surrounded by a fluid, and a hyperelastic rectangle in a time-varying shear flow.

In this study, a high viscosity is attributed to the solid zone which resolves the nonphysical dynamic condition at the fluid/solid interface. From extensive numerical simulations performed in the course of this study, it was found that the ratio of solid-to-fluid viscosities should be almost the same as the ratio of solid-to-fluid densities.

5.1 Motion and Impact of a Hyperelastic Sphere Onto a Rigid Substrate. A sphere made of silicone moves in air and impacts onto a rigid substrate. The surface roughness of the substrate and that of the sphere are not considered in the model. Silicon has been reported to behave as a hyperelastic material [32]; therefore, the silicon sphere is modeled based on the neo-Hookean constitutive equation for which the hyperelasatic treatment of Marckmann and Verron [33] can be used. The neo-Hookean model involves only one unknown parameter and can be used to predict the material responses with small deformations under different types of loading conditions.

A schematic of the problem and its initial condition considered for simulations are shown in Fig. 4. The initial conditions and the properties are as follows:

Sphere radius: 19.2 mm
Initial position of the sphere: 57.3 mm
Initial velocity of the sphere: 1.22 m/s
Solid density: 1106 kg/m^3

The size of the computational domain, 45 mm in radial and 90 mm in axial direction, was large enough to encompass both the initial sphere and its subsequent deformations. The discretization of the domain was performed using a uniform mesh. The mesh size can be characterized based on the sphere radius using a parameter called CPR (number of cells per radius). A mesh refinement study was performed in which the grid size was gradually reduced until no significant changes were seen in the simulation results for the sphere deformation. The results of this study are presented in Fig. 5 where the position of the center of the sphere volume and the axial velocity are displayed. Before

Table 1 Equipment and their uncertainties

	Device	Accuracy (unit)	Uncertainty (unit)
Image	CCD camera (grasshopper, Canada)	±5 (pixel)/±0.02 (mm)	1 (pixel)/0.001 (mm)
Length	Digital caliper	±(0.02) (mm)	0.006 (mm)
Mass	Digital balance	±(0.02) (g)	0.006 (g)

the sphere impact onto the substrate, the sphere is moving as a solid with the initial specified velocity. Therefore, no significant differences are observed between the results for different mesh sizes. After the impact and bouncing, however, the effect of the mesh size is clearly observed. A close inspection of the simulations revealed that the differences in the results were due to the elastic term of the momentum equation. When the sphere impacts onto the rigid substrate its kinetic energy converts to the elastic potential which is a functional of the left Cauchy-Green deformation tensor. For a mesh size coarser than 35 CPR, the calculation of this deformation tensor is not sufficiently accurate which results in an under estimated bouncing velocity of the sphere. However, as shown in Fig. 5, for a mesh size finer than 35 CPR, no more significant changes are seen in the results for both sphere position (Fig. 5(*a*)) and the axial velocity (Fig. 5(*b*)). A mesh size of 35 CPR, therefore, was selected for the rest of simulations in this case.

Figure 6 shows the numerical and experimental results of the sphere before, during and after the impact. Particulary, the results during the imapct and rebound were of interest where there are rapid changes in the velocity of both solid and surrounding fluid. The rapid changes of the fluid velcoity leads to viscous dissipiation which damps the solid velocity during a very short time after the rebound. In Fig. 6, the numerical results are presented in both 3D views and 2D cross sections. In the cross-sectional views, both the streamline (right of each image) and velocity vectors (left of each image) are shown in different locations of the solid to give a better insight of the air and solid motion. At $t = 31.5$ ms, the sphere has reached almost a zero velocity and the air between the sphere and the substrate is pushed away. A better display of the numerical results especially for comparison with those of the experiments can be obtained by 3D views of the phenomenon; this is accomplished by rotating the 2D results about axial direction (*y*-axis in Fig. 4). A good qualitative agreement is observed in Fig. 6 between the results of simulations and experiments. It is worth emphasizing that in the FSI treatment used in this study although the solid body is modeled as a high viscous fluid, the elastic stresses are considered in the simulations as explained before. This leads to the fact the solid body is treated as a deformable body in the simulation and that is why the silicon sphere in Fig. 6 bounces back after its impact on the rigid substrate. If the solid body was only treated as a high viscous fluid with no further considerations as introduced in previous studies in the literature [25,26], the sphere after the impact would stay on the substrate and would not bounce back.

Figure 7 displays a quantitative comparison between numerical and experimental results for the position of the center of the sphere volume and the axial velocity. An excellent agreement between numerical and experimental results is demonstrated, showing that the present numerical method is able to capture the motion of solid object in fluid (air). By a comparison of the numerical and experimental results, the unknown coefficient of the solid is found to be: $G = 0.18$ MPa. (G denotes the modulus of the transverse elasticity for the neo-Hookean material).

To examine the validity of the obtained coefficient ($G = 0.18$ MPa), two more cases given in Table 2 with different initial positions and velocities are studied. The same value of G as of the previous case is used in the numerical model. The comparison between simulations and measurements for these cases are

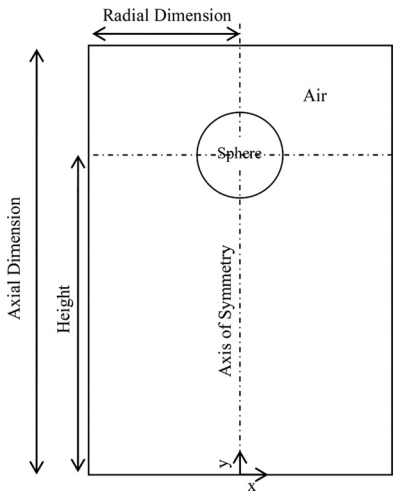

Fig. 4 Schematic of a sphere during its motion in air and the initial and boundary conditions for the simulation

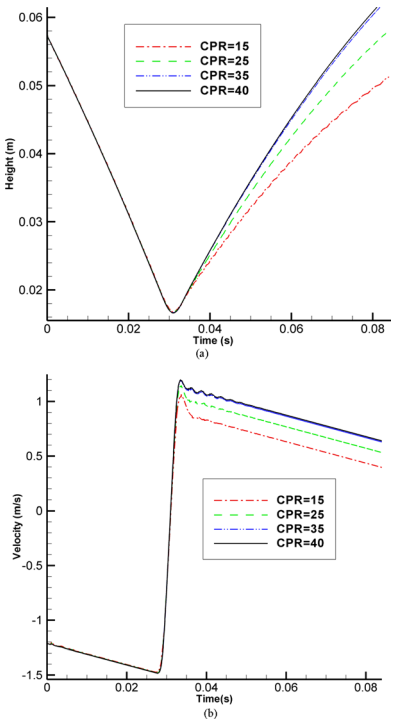

Fig. 5 The result of mesh refinement study for (*a*) the position of the center of the sphere volume versus time and (*b*) the axial velocity versus time. The mesh size is characterized based on the number of CPR of the solid.

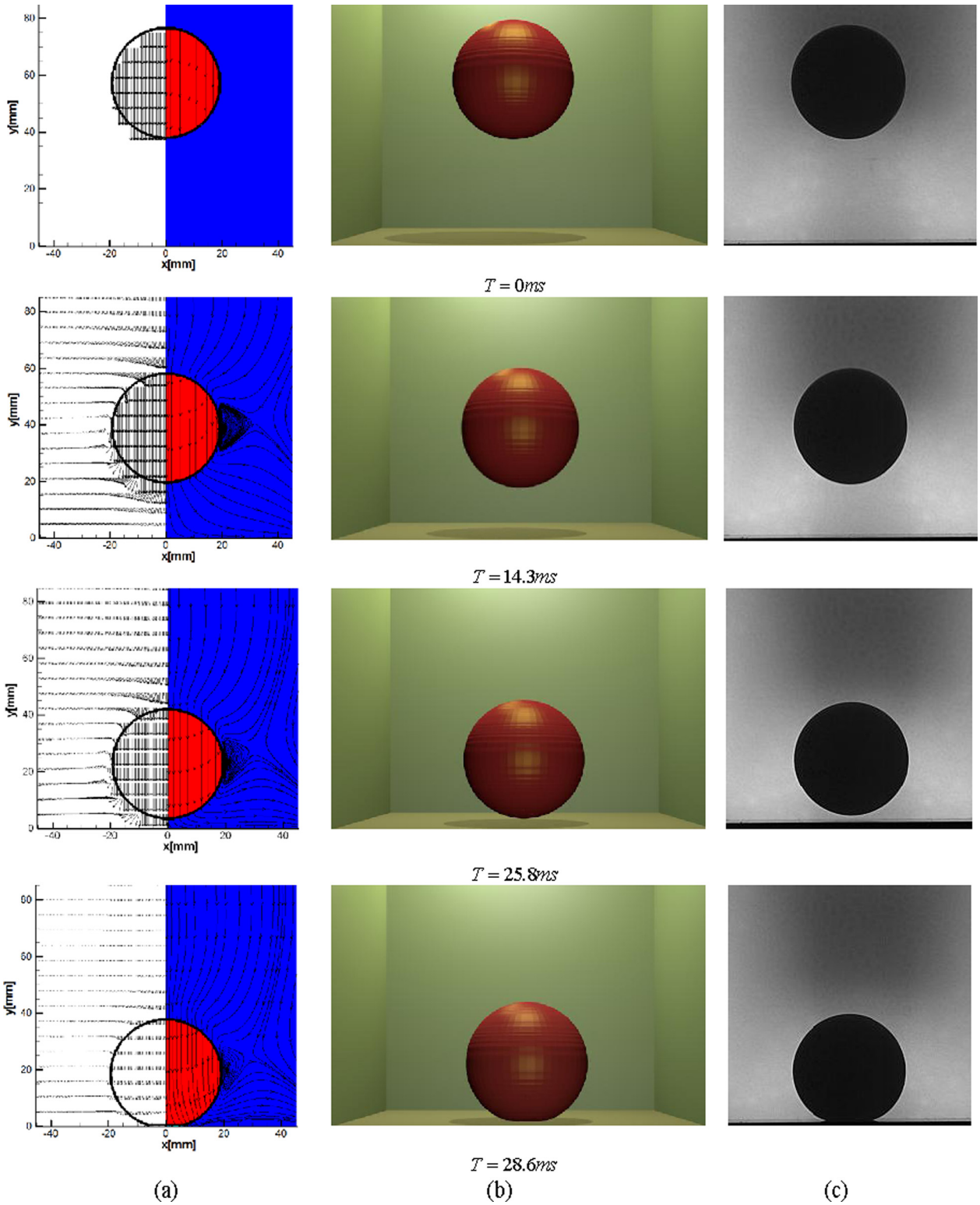

Fig. 6 The evolution of the motion and impact of a hyperelastic sphere with a radius 19.2 mm and a density 1106 kg/m^3 in air onto a rigid substrate from the present model for (*a*) cross-sectional images, (*b*) 3D views, and (*c*) experimental results performed in this study

displayed in Fig. 8 which indicates a good agreement between the results of the model and experiments.

5.2 Deformation of a Soft Wall in a Fluid Flow. Wang and Zhang [34] considered a cavity 2×2 cm where the bottom up to the height of 0.5 cm was occupied by a neo-Hookean solid and the rest of the cavity was filled with a fluid. In their simulations, the velocities were zero at all cavity boundaries except the top lid, where the x component of the velocity was

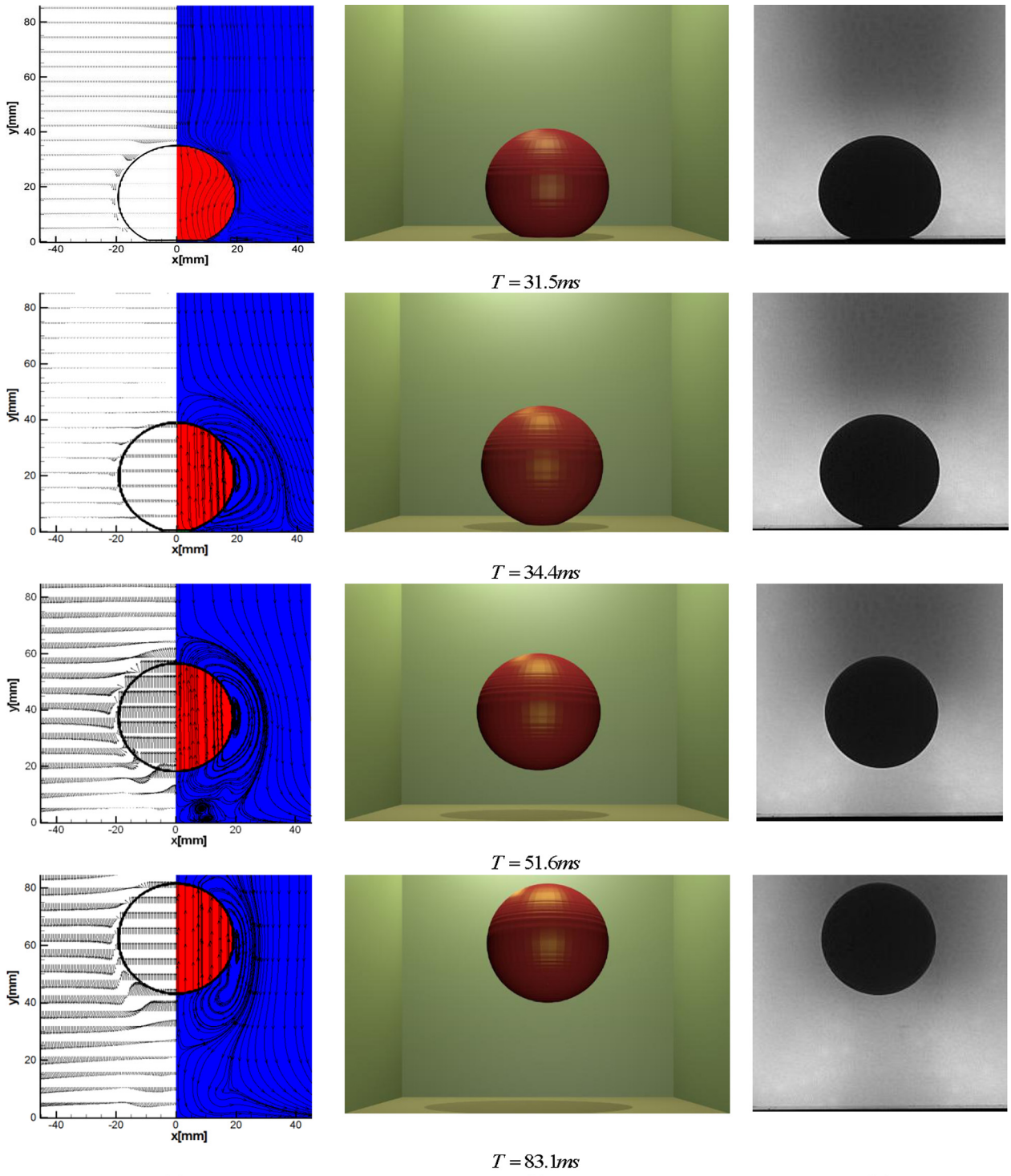

Fig. 6 (Continued)

$$u = 0.5\begin{cases} \sin^2\left(\dfrac{\pi x}{0.6}\right) & x \in [0.0, 0.3] \\ 1 & x \in (0.3, 1.7) \\ \sin^2\left(\dfrac{\pi(x-2)}{0.6}\right) & x \in [1.7, 2.0] \end{cases} \tag{26}$$

The fluid and solid densities were considered the same equal to one. The fluid dynamic viscosity was assumed $\mu_1 = 0.2$ and the solid coefficient $G = 0.2$. They neglected the advection terms in the Navier–Stokes equation [34]. The same case with exactly the same geometry, same material properties and boundary conditions were tested using the developed model in this study. The results of this simulation along with those of Wang and Zhang [34] are presented in Fig. 9. The deformed solid reaches a steady state at $t = 8$ s, when a vortex is formed in the middle of the fluid domain. The wall deformation and the streamlines shown in Fig. 9 reveals a good agreement with the simulations performed in this study and those reported by Wang and Zhang [34].

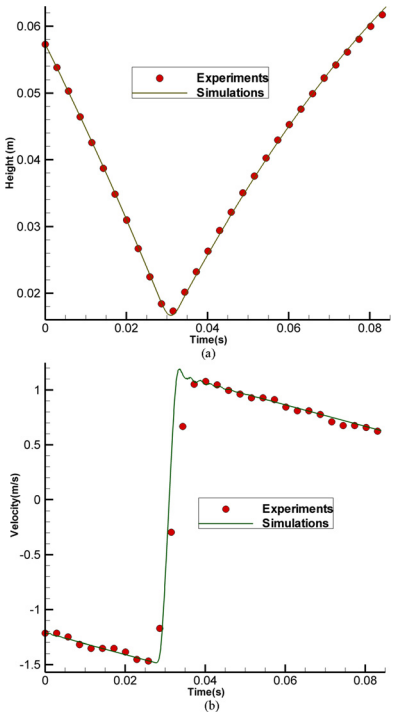

Fig. 7 Comparison of the numerical results with those of the experiments for (*a*) the position of the center of sphere volume and (*b*) the axial velocity

5.3 Motion of a Solid in a Lid-Driven Cavity Flow. Zhao et al. [35] studied the simulation of a deformable solid motion in a lid-driven cavity flow. The size of the cavity was 1×1 m and initially the system was at rest. The unstressed solid object was a disk with a radius of 0.2 m centered at (0.6, 0.5). The no-slip condition was imposed on the walls. At $t = 0$, to drive the fluid and solid motions, the top wall started to move at a speed of $V_{\text{wall}} = 1$ m/s in x direction. The model used to treat the solid component was that of a neo-Hookean material. The solid and fluid properties were $\rho_l = \rho_s = 1$, $\mu_l = 0.01$, and $G = 0.1$. Figure 10 displays a comparison between the results of simulations performed in this study for exactly the same scenario with those of Zhao et al. [35]. The disk moves and deforms by the fluid flow, and as it approaches the top wall, more deformation is exhibited. The deformation of the solid object (disk) is not symmetric about its vertical centerline. Therefore, downward force which called lubrication force is produced in gap between the solid and top wall of cavity [35]. This force acting on the solid prevents the object from touching the top wall of the cavity. As observed in Fig. 10, a close agreement exists between the shape and flow streamlines from this study with those reported by Zhao et al. [35].

5.4 Oscillating Disk in a Preset Velocity Field. Robinson et al. [36] considered a circular deformable body placed within a fluid domain of dimensions 1×1 m with no slip boundary conditions. An initial velocity was imposed in both the fluid and solid body based on the stream function $\psi = 0.05 \sin(2\pi x)\sin(2\pi y)$. A neo-Hookean constitutive model was used for the solid with $G = 1$. The fluid and solid properties were $\rho_l = \rho_s = 1$ and $\mu_l = 0.001$. The simulations were run for a period of 1 s. The disk was initially stressed free and its undeformed shape was a circle. The results of simulations along with those of Robinson et al. [36] are shown in Fig. 11. The system gradually changes like a damped oscillator without any external forcing. At $t = 0.2$ s, the maximum deformation occurs. As seen in the figure at $t = 0.5$ s, two vortices exist in the fluid flow in each quarter: one in the fluid domain and the other at the fluid/solid interface. Figure 11 shows a good agreement between the results of the present study with those reported by Robinson et al. [36].

Table 2 Initial velocities and positions (height) of the sphere for two different cases

	Case (1)	Case (2)
Initial position (mm)	61.9	58.6
Initial velocity (m/s)	0.73	1.06

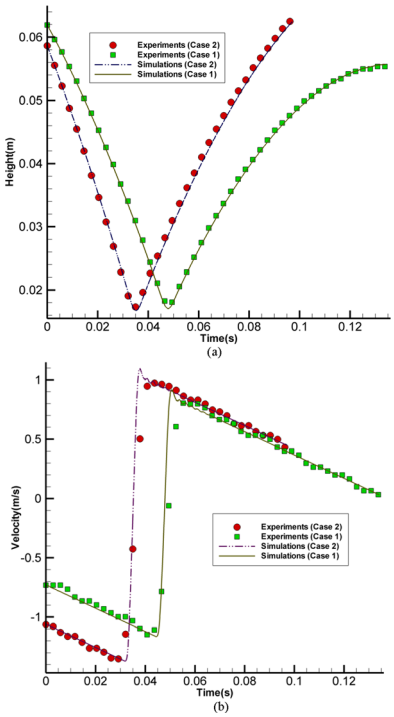

Fig. 8 Comparison of the numerical results with those of the experiments for various initial positions and velocities of the sphere: (*a*) the position of center of the sphere volume and (*b*) the axial velocity

5.5 Hyperelastic Material in a Time-Varying Shear Flow. When a hyperelastic material after being deformed in a fluid flow is set free from stresses, it usually shows reversibility toward the initial shape [19,23]. In this section, a hyperelastic rectangle is

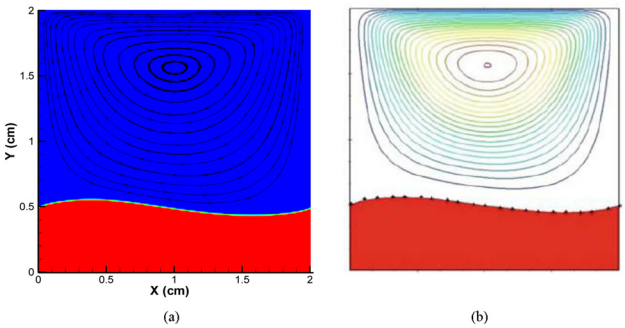

Fig. 9 The simulation results for a soft wall in a lid-driven cavity flow from (*a*) present study and (*b*) those of Wang et al. [34]. (Reprinted with permission from Springer Science and Business Media.)

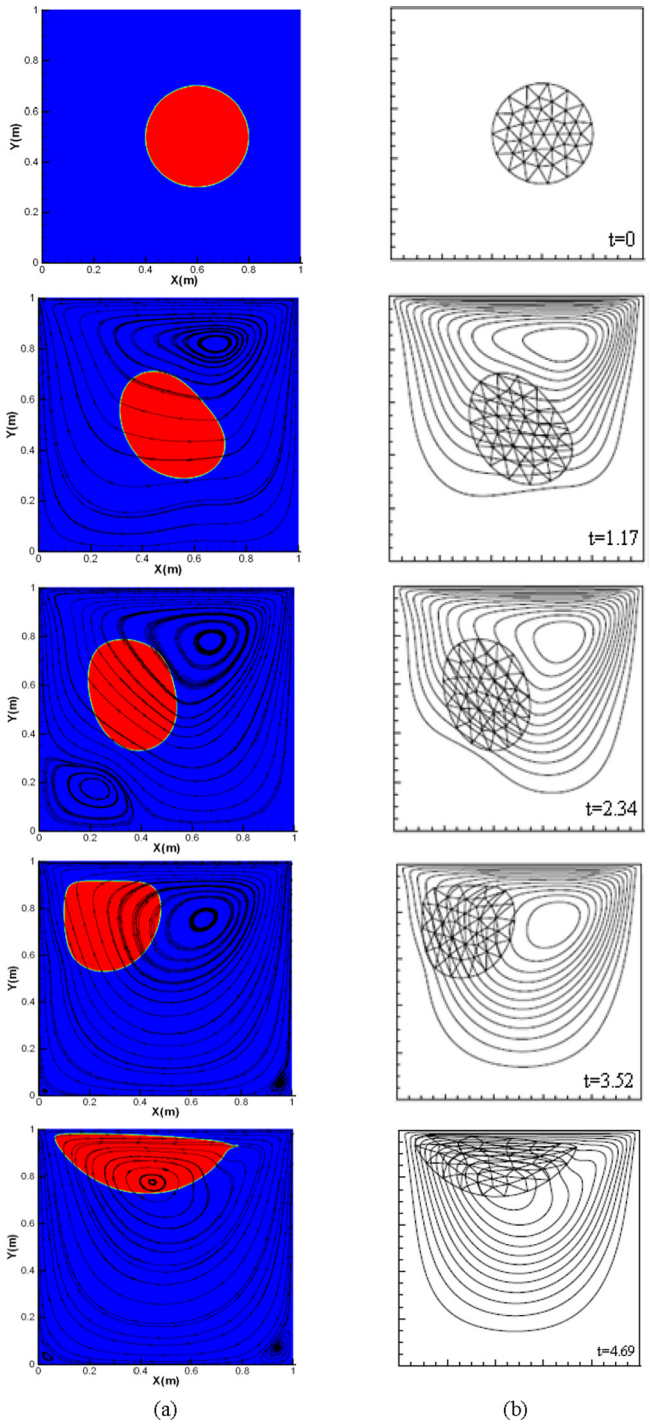

Fig. 10 The simulation results for a deformable solid motion in a lid-driven cavity flow from (*a*) present study and (*b*) those of Zhao et al. [35]. (Reprinted with permission from Elsevier.)

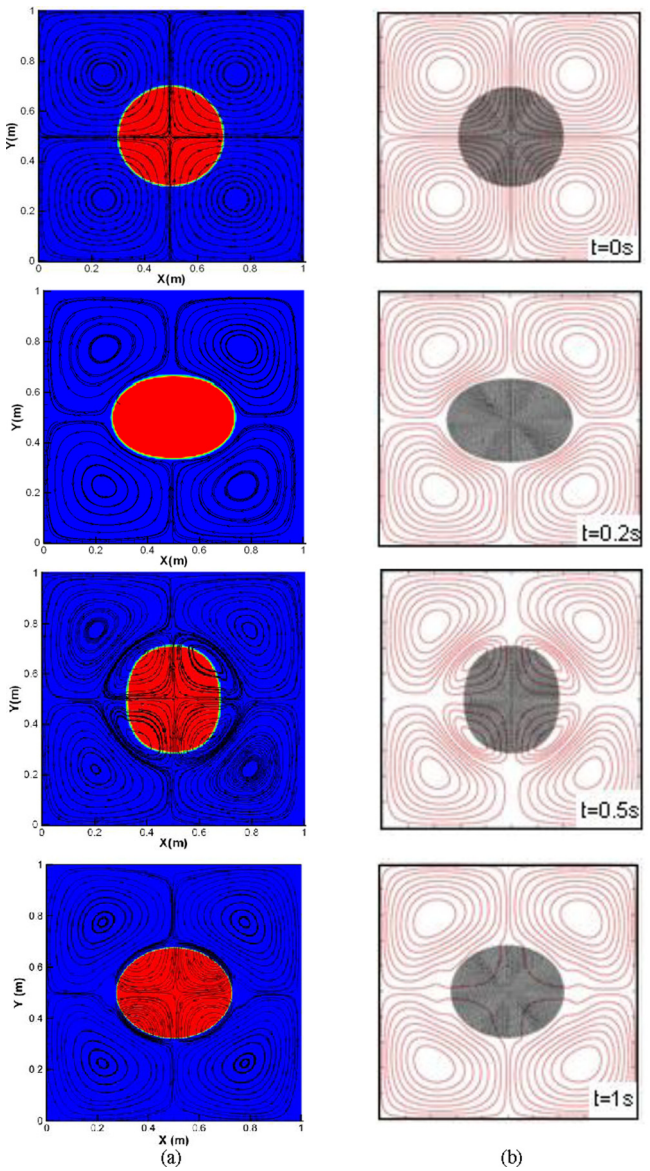

Fig. 11 The simulation results for an oscillating disk in fluid from (*a*) present study and (*b*) those of Robinson et al. [36]. (Reprinted with permission from Elsevier.)

modeled in a time-varying shear flow similar to the case considered by Sugiyama et al. [19] to estimate the reversibility of the hyperelastic material using an Eulerian method. In this case, a Couette flow between two flat plates involving the Saint Venant-Kirchhoff material with a dimension of 2.375×1 m is considered. The solid object with properties $\rho_s = 1$, $\lambda^s_{\text{Lame}} = 6$, and $\mu^s_{\text{Lame}} = 4$ (i.e., $C_1 = 4$, $C_2 = -2$, and $C_3 = 1.75$) immersed in a fluid with $\rho_l = 1$ and $\mu_l = 1$. The upper and lower plates were located at $y = 2$ and $y = 0$ and the computational extent in the x direction was set to 8 m. Initially, the system was at rest. Within a period of $0 \le t \le 4$ s, the upper and lower plates moved at a velocity of $V_w^{\text{upper}} = 1$ m/s and $V_w^{\text{lower}} = -1$ m/s in the x direction. After $t = 4$ s, the moving plates are stopped to release the solid object from the shearing force. Figure 12 displays the solid deformation in six time instants from the simulations performed in this study and those reported by Sugiyama et al. [19]. As the shear flow is induced by the moving plates, the shearing force causes the solid to extend in the horizontal direction. At $t = 4$ s, the left-top and right-bottom corners of the solid object are largely deformed. After this time, the fluid flow rapidly decays and the deformed solid gradually recovers the initial shape. A good comparison is seen between the results of the present study with those of Sugiyama et al. [19].

6 Conclusion

A full Eulerian simulation method for solving FSI problems in various 2D/axisymmetric scenarios was developed. The developed model uses an Eulerian approach for both fluid and

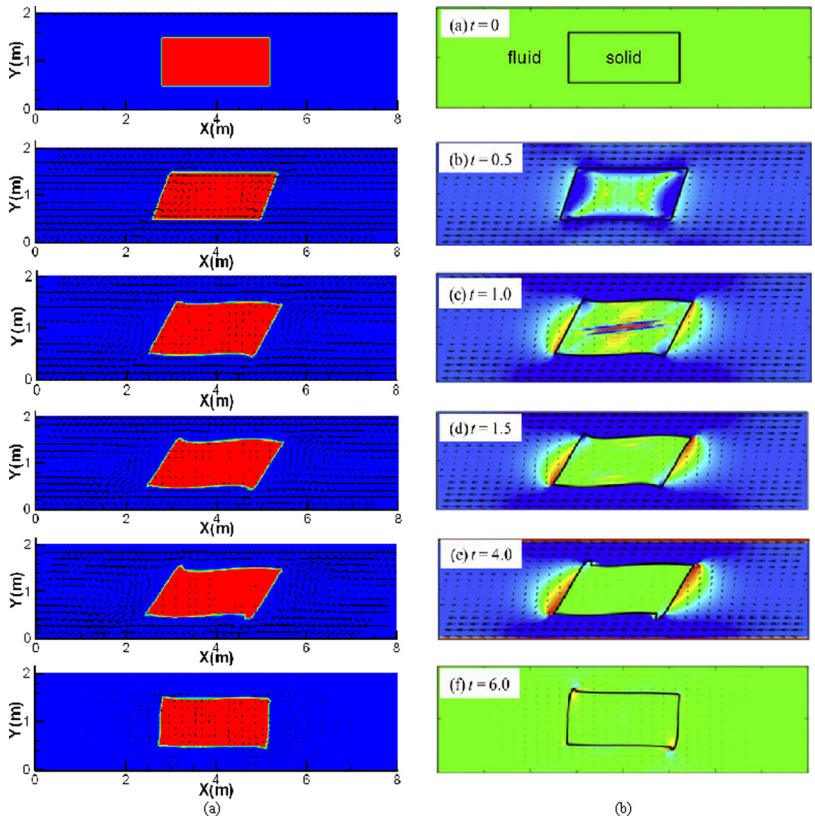

Fig. 12 The hyperelastic rectangle in a time-varying shear flow: (*a*) present study and (*b*) those of Sugiyama et al. [19]. (Reprinted with permission from Elsevier.)

deformable solid and the VOF method to obtain the position of the solid object. The temporal change in solid deformation was calculated by updating a deformation tensor. An implicit formulation for the elastic stress was used through a fourth-order Jacobian tensor to avoid the instability for high stiff solid objects. The elastic stresses have discontinuities across the fluid/solid interface. Therefore, the dynamic boundary condition was not completely satisfied. For improving this boundary condition, the viscosity in the solid object was increased which reduced the effects of the elastic stresses in the fluid/solid interface resulting in a stable simulation. As a result, compared to other available methods for modeling FSI, the presented algorithm is more efficient and needs less computational time and effort.

For validating the numerical results, an experiment was performed in which the movement of a spherical deformable solid object in air and its impact onto a rigid substrate were studied. In the experiment, a CCD camera was employed to capture images from the movement of the sphere. Next, the image processing technique was used to obtain the position of the sphere and its velocity. The numerical results for the same problem compared well with those of the experiments both qualitatively and quantitatively.

Further validation of the model was performed by a comparison of the simulation results for FSI scenarios for which other numerical results were available in the literature. These cases included the deformation of a deformable wall by a fluid flow in a 2D cavity; the motion of a deformable solid object in a 2D cavity; the motion of a deformable disk in surroundings fluid by enforcing an initial oscillating movement; and the motion of a hyperelastic material in a time-varying shear flow. For all cases, the numerical results were in good agreement with available results in the literature.

Acknowledgment

This work was supported in part by Ferdowsi University of Mashhad's Research Council, under Grant No. 3/24112 (Dec. 3, 2013) on Static Fine Job.

References

[1] Belytschko, T., and Kennedy, J., 1975, "Finite Element Approach to Pressure Wave Attenuation by Reactor Fuel Subassemblies," ASME J. Pressure Wave Technol., **97**(3), pp. 172–177.
[2] Donea, J., Fasoli-Stella, P., and Giuliani, S., 1976, "Finite Element Solution of Transient Fluid-Structure Problems in Lagrangian Coordinates," International Meeting on Fast Reactor Safety and Related Physics, Chicago, IL, Oct. 8, Vol. 3, pp. 1427–1435.
[3] Hirt, C., Amsden, A., and Cook, J., 1974, "An Arbitrary Lagrangian–Eulerian Computing Method for all Flow Speeds," J. Comput. Phys., **14**(3), pp. 227–253.
[4] Nitikitpaiboon, C., and Bathe, K., 1993, "An Arbitrary Lagrangian–Eulerian Velocity Potential Formulation for Fluid-Structure Interaction," Comput. Struct., **47**(5), pp. 871–891.
[5] Figueroa, C., Vignon, I., Jansen, K., Hughes, T., and Taylor, C., 2006, "A Coupled Momentum Method for Modeling Blood Flow in Three-Dimensional Deformable Arteries," J. Comput. Methods Appl. Mech. Eng., **195**(41–43), pp. 1–22.
[6] Hu, H., 1996, "Direct Simulation of Flows of Solid-Liquid Mixtures," Int. J. Multiphase Flow, **22**(2), pp. 335–352.
[7] Gao, T., and Hu, H., 2009, "Deformation of Elastic Particles in Viscous Shear Flow," J. Comput. Phys., **228**, pp. 2132–2151.
[8] Haug, E. J., 1992, *Intermediate Dynamics*, Prentice Hall, Englewood Cliffs, NJ.
[9] Wang, X., Wang, C., and Zhang, L. T., 2012, "Semi Implicit Formulation of the Immersed Finite Element Method," J. Comput. Mech., **49**, pp. 421–430.
[10] Peskin, C., 1972, "Flow Patterns Around Heart Valves: A Numerical Method," J. Comput. Phys., **10**, pp. 252–271.
[11] Wang, X. S., and Liu, W. K., 2004, "Extended Immersed Boundary Method Using FEM and RKPM," Comput. Methods Appl. Mech. Eng., **193**, pp. 1305–1321.
[12] Gilmanov, A., and Acharya, S., 2008, "A Hybrid Immersed Boundary and Material Point Method for Simulating 3D Fluid-Structure Interaction Problems," Int. J. Numer. Methods Fluids, **56**, pp. 151–177.

[13] Le, D. V., Khoo, B. C., and Peraire, J., 2006, "An Immersed Interface Method for Viscous Incompressible Flows Involving Rigid and Flexible Boundaries," J. Comput. Phys., **220**, pp. 109–138.
[14] Glowinski, R., Pan, T., Hesla, T., and Joseph, D., 1999, "A Distributed Lagrange Multiplier/Fictitious Domain Method for Particulate Flows," Int. J. Multiphase Flow, **25**, pp. 755–794.
[15] Hoogstraten, P., Slaats, P., and Baijens, F., 1991, "An Eulerian Approach to the Finite Element Modeling of Neo-Hookean Rubber Material," Appl. Sci. Res., **48**, pp. 193–210.
[16] Liu, C., and Walkington, N., 2001, "An Eulerian Description of Fluids Containing Visco-Elastic Particles," Arch. Ratio. Mech. Anal., **159**, pp. 229–252.
[17] Sugiyama, K., Ii, S., Takeuchi, S., Takagi, S., and Matsumoto, Y., 2010, "Full Eulerian Simulation of Biconcave Neo-Hookean Particles in a Poiseuille Flow," J. Comput. Mech., **46**, pp. 147–157.
[18] Nagano, N., Sugiyama, K., Takeuchi, S., Ii, S., Takagi, S., and Matsumoto, Y., 2010, "Full Eulerian Finite Difference Simulation of Fluid Flow in Hyperelastic Wavy Channel," J. Fluid Sci. Technol., **5**(3), pp. 475–490.
[19] Sugiyama, K., Ii, S., Takeuchi, S., Takagi, S., and Matsumoto, Y., 2011, "A Full Eulerian Finite Difference Approach for Solving Fluid-Structure Coupling Problems," J. Comput. Phys., **230**, pp. 596–627.
[20] Ii, S., Sugiyama, K., Takeuchi, S., Takagi, S., and Matsumoto, Y., 2011, "An Implicit Full Eulerian Method for the Fluid-Structure Interaction Problem," Int. J. Numer. Methods Fluids, **65**, pp. 150–165.
[21] Sugiyama, K., Nagano, N., Takeuchi, S., Ii, S., Takagi, S., and Matsumoto, Y., 2011, "Particle-in-Cell Method for Fluid-Structure Interaction Simulations of Neo-Hookean Tube Flows," Theor. Appl. Mech., **59**, pp. 245–256.
[22] Ii, S., Gong, X., Sugiyama, K., Wu, J., Huang, H., and Takagi, S., 2011, "A Full Eulerian Fluid-Membrane Coupling Method With a Smoothed Volume of Fluid Approach," J. Comput. Phys., **69**, pp. 1–33.
[23] Takagi, S., Sugiyama, K., Ii, S., and Matsumoto, Y., 2012, "A Review of Full Eulerian Methods for Fluid-Structure Interaction Problems," ASME J. Appl. Mech., **79**, pp. 1–18.
[24] Ii, S., Sugiyama, K., Takagi, S., and Matsumoto, Y., 2012, "A Computational Blood Flow Analysis in a Capillary Vessel Including Multiple Red Blood Cells and Platelets," J. Biomech. Sci. Eng., **7**(1), pp. 72–83.
[25] Mirzaii, I., and Passandideh-Fard, M., 2012, "Modeling Free Surface Flows in Presence of an Arbitrary Moving Object," Int. J. Multiphase Flow, **39**, pp. 216–226.
[26] Carlson, M., Mucha, P., Brooks, R., and Turk, G., 2002, "Melting and Flowing," ACM SIGGRAPH, 2002 Symposium on Computer Animation, San Antonio, TX, July 21–22, pp. 167–174.
[27] Youngs, D. L., 1984, "An Interface Tracking Method for a 3D Eulerian Hydrodynamics Code," AWRE, Technical Report No. 44/2092/35.
[28] Bonet, J., and Wood, R., 1997, *Nonlinear Continuum Mechanics for Finite Element Analysis*, 2nd ed., Cambridge University, Cambridge, New York.
[29] Chang, Y., Bao, K., Zhu, J., and Wu, E., 2011, "High Viscosity Fluid Simulation Using Particle-Based Method," IEEE International Symposium on Virtual Reality Innovation, Singapore, March 19–20, pp. 199–205.
[30] Kershaw, D. S., 1978, "The Incomplete Cholesky-Conjugate Gradient Method for the Iterative Solution of Systems of Linear Equations," J. Comput. Phys., **26**(1), pp. 43–65.
[31] Sardarabadi, M., Passandideh-Fard, M., and Zeinali Heris, S., 2014, "Experimental Investigation of the Effects of Silica/Water Nanofluid on PV/T (Photovoltaic Thermal Units)," J. Energy, **66**, pp. 264–272.
[32] Darkner, S., and Erleben, K., 2011, "A Hyperelasticity Method for Interactive Virtual Design of Hearing Aids," J. Visual Comput., **27**, pp. 645–653.
[33] Marckmann, G., and Verron, E., 2006, "Comparison of Hyperelastic Models for Rubber-Like Materials," Rubber Chem. Technol., **79**, pp. 835–858.
[34] Wang, X., and Zhang, L., 2010, "Interpolation Functions in the Immersed Boundary and Finite Element Methods," J. Comput. Mech., **45**, pp. 321–334.
[35] Zhao, H., Freund, J. B., and Moser, R. D., 2008, "A Fixed-Mesh Method for Incompressible Flow-Structure Systems With Finite Solid Deformations," J. Comput. Phys., **227**, pp. 3114–3140.
[36] Robinson, A., Schroeder, C., and Fedkiw, R., 2011, "A Symmetric Positive Definite Formulation for Monolithic Fluid-Structure Interaction," J. Comput. Phys., **230**, pp. 1547–1566.